

X-Ray and Optical Microlensing in the Lensed Quasar PG 1115+080¹

Christopher W. Morgan^{2,3}, Christopher.S. Kochanek^{3,4}, Xinyu Dai^{3,4}, Nicholas D. Morgan³
and Emilio E. Falco⁵

ABSTRACT

We analyzed the microlensing of the X-ray and optical emission of the lensed quasar PG 1115+080. We find that the effective radius of the X-ray emission is $1.2_{-0.4}^{+0.7}$ dex smaller than that of the optical emission. Viewed as a thin disk observed at inclination angle i , the optical accretion disk has a scale length, defined by the point where the disk temperature matches the rest frame energy of the monitoring band ($kT = hc/\lambda_{rest}$ with $\lambda_{rest} = 0.3\mu\text{m}$), of $\log[(r_{s,opt}/\text{cm})\sqrt{\cos(i)/0.5}] = 16.2 \pm 0.3$. The X-ray emission region (1.4-21.8 keV in the rest frame) has an effective half-light radius of $\log[r_{1/2,X}/\text{cm}] = 15.3_{-0.6}^{+0.5}$. Given an estimated black hole mass of $1.23 \times 10^9 M_{\odot}$, corresponding to a gravitational radius of $\log[r_g/\text{cm}] = 14.3$, the X-ray emission is generated near the inner edge of the disk while the optical emission comes from scales slightly larger than those expected for an Eddington-limited thin disk. We find a weak trend supporting models with low stellar mass fractions near the lensed images, in mild contradiction to inferences from the stellar velocity dispersion and the time delays.

¹Based on observations obtained with the Small and Moderate Aperture Research Telescope System (SMARTS) 1.3m, which is operated by the SMARTS Consortium, the Apache Point Observatory 3.5-meter telescope, which is owned and operated by the Astrophysical Research Consortium, the WIYN Observatory which is owned and operated by the University of Wisconsin, Indiana University, Yale University and the National Optical Astronomy Observatories (NOAO), the 6.5m Magellan Baade telescope, which is a collaboration between the observatories of the Carnegie Institution of Washington (OCIW), University of Arizona, Harvard University, University of Michigan, and Massachusetts Institute of Technology, and observations made with the NASA/ESA Hubble Space Telescope for program HST-GO-9744 of the Space Telescope Science Institute, which is operated by the Association of Universities for Research in Astronomy, Inc., under NASA contract NAS 5-26555.

²Department of Physics, United States Naval Academy, 572C Holloway Road, Annapolis, MD 21402

³Department of Astronomy, The Ohio State University, 140 West 18th Avenue, Columbus, OH 43210-1173

⁴Center for Cosmology and AstroParticle Physics, The Ohio State University

⁵Harvard-Smithsonian Center for Astrophysics, 60 Garden Street, Cambridge, MA, 02138

Subject headings: accretion, accretion disks — dark matter — gravitational lensing — quasars: general — Xrays:quasars

1. Introduction

When Blaes (2007) recently reviewed the state of accretion disk physics, he found that one of the most glaring problems in even the most sophisticated accretion disk models (e.g. Hubeny et al. 2000, 2001; Hirose, Krolik & Stone 2006) is their failure to support a hot corona or to produce X-rays at all. While there are models for producing the X-rays, (e.g. Haardt & Maraschi 1991, 1993; Maraschi & Tavecchio 2003; Hirose et al. 2004; Nayakshin, Cuadra & Springel 2007), they do so on very different physical scales relative to the gravitational radius $r_g = GM_{BH}/c^2$ of the black hole. For example, the magnetohydrodynamic (MHD) simulations of Hawley & Balbus (2002) predict the dragging of hot ionized gas from a jet across the surface of a cooler accretion disk resulting in bremsstrahlung. In this model, much of the emission comes from an inner torus with radius $r \lesssim 20r_g$, but the continuum emission region extends to very large radii ($r \approx 200r_g$). On much smaller scales, the model of Hirose et al. (2004) suggests a relativistic MHD accretion disk model in the Kerr metric whose inner torus ($r \lesssim 10r_g$) supports a large current density capable of emitting a moderate X-ray flux. The disk-corona model of Haardt & Maraschi (1991, see also Merloni 2003) produces X-rays via inverse Compton scattering in a corona which extends over much of the optical/UV accretion disk, while the “lamp-post” (Martocchia et al. 2002) and “aborted jet” (Ghisellini et al. 2004) models predict a significantly smaller emission structure ($r \lesssim 3.0r_g$).

Given their small angular size, few traditional observational constraints can be placed on the size of quasar X-ray continuum emission regions apart from simple and often inconclusive variability timescale arguments (e.g. Vaughan, Fabian & Nandra 2003). Fabian et al. (1995) demonstrated that the broad Fe K α X-ray emission line in Seyfert 1 spectra is probably emitted from the region immediately surrounding the black hole. The width and variability of Fe K α emission has now been measured in a number of systems to study the innermost regions of those accretion disks (e.g. Iwasawa et al. 1999; Lee et al. 1999; Fabian et al. 2002; Iwasawa et al. 2004). Motivated by this work, Young & Reynolds (2000); Ballantyne et al. (2005) and others have proposed the use of *Constellation-X* to measure the size of the Fe K α X-ray reflection region by reverberation mapping. Fortunately, gravitationally lensed quasars can be studied on these scales at all wavelengths because the quasar is microlensed by the stars in the lens galaxy. The Einstein radius R_E of the stars is comparable to the expected near-IR sizes of accretion disks, so most disk emission will be significantly

microlensed with the amplitude of the variability increasing rapidly for source components that are small compared to R_E due to the presence of caustic curves on which the microlensing magnification diverges (see the review by Wambsganss 2006).

More generally, microlensing variability is a function of the relative tangential velocity v_e between source, lens and observer, the macroscopic lensing properties of the lens galaxy (the convergence κ , the stellar surface density fraction κ_*/κ and the shear γ) and the relative sizes of the source and the source plane projection of the Einstein radius R_E of an average mass star $\langle M \rangle$ in the lens galaxy. Since the size of the X-ray emitting region is expected to be much smaller than the optical accretion disk, we expect that the effects of microlensing will be more pronounced at X-ray wavelengths than in the optical (e.g. Jovanović et al. 2008). This effect has now been observed in many lensed quasars (e.g. Morgan et al. 2001; Chartas et al. 2002; Dai et al. 2003; Blackburne et al. 2006; Chartas et al. 2007; Pooley et al. 2007) and was documented specifically in PG 1115+080 by Pooley et al. (2006).

The quadruply-lensed quasar PG 1115+080 was discovered over 25 years ago (Weymann et al. 1980). Since then, it has been the subject of a large number of investigations at multiple wavelengths. In particular, the closely separated A1 and A2 images bracket a critical line so we expect their flux ratio to be approximately unity, but Impey et al. (1998) and others have measured an anomalously low flux ratio in the optical and NIR (e.g. $A2/A1 = 0.64 \pm 0.02$ in the H -band). Chiba et al. (2005) showed that the $A2/A1$ flux ratio returns to nearly unity in the mid-IR ($A2/A1 = 0.93 \pm 0.06$ at $11.7\mu\text{m}$), demonstrating that stellar microlensing is the likely cause of the anomaly rather than millilensing (e.g. Kochanek & Dalal 2004). Furthermore, in this paper we report a change of ~ 0.2 mag in $A2/A1$ during the last three seasons of our monitoring campaign, providing additional evidence that microlensing is the source of the anomaly.

Recently, Pooley et al. (2006) conducted a study of the system’s anomalous X-ray flux ratios as measured in two *Chandra X-Ray Observatory* (*Chandra*) observations. Pooley et al. (2006) demonstrated that microlensing is the likely cause of the X-ray flux ratio anomaly in PG 1115+080 and qualitatively argued that its X-ray continuum emission region must be significantly smaller than its optical accretion disk. In this paper, we combine these 2 epochs of X-ray data from *Chandra* with our optical monitoring data to make simultaneous measurements of the system’s optical and X-ray continuum emission regions using the Monte Carlo microlensing analysis technique of Kochanek (2004).

In § 2, we describe our optical monitoring data and the X-ray flux measurements. In § 3, we review our microlensing analysis technique and describe its application to PG 1115+080. In § 4 we present the results of our calculations and discuss their implications for the sizes of the quasar emission regions and the stellar content of the lens galaxy. We assume a flat

cosmology with $\Omega_0 = 0.3$, $\Lambda_0 = 0.7$ and $H_0 = 70 \text{ km s}^{-1} \text{ Mpc}^{-1}$.

2. *Hubble Space Telescope Observations, Chandra and Optical Monitoring Data*

We observed PG 1115+080 in the *V*- (F555W), *I*- (F814W) and *H*- (F160W) bands using the *Hubble Space Telescope* (*HST*) for the CfA-Arizona Space Telescope Survey (CASTLES¹, Falco et al. 2001). The *V*- and *I*-band images were taken using the Wide-Field Planetary Camera 2 (WFPC2). The *H*-band images, originally reported in Yoo et al. (2005), were taken using the Near-Infrared Camera and Multi-Object Spectrograph (NICMOS). We made photometric and astrometric fits to the *HST* imagery with *imfitfits* (Lehár et al. 2000), using a de Vaucouleurs model for the lens galaxy, an exponential disk model for the quasar host galaxy and point sources for the quasar images. The astrometric fits are consistent with those of Impey et al. (1998). Our *HST* astrometry and photometry are presented in Table 1.

We monitored PG 1115+080 in the *R*-band over multiple seasons with the SMARTS 1.3m telescope using the ANDICAM optical/infrared camera (DePoy et al. 2003)², the Wisconsin-Yale-Indiana (WIYN) observatory using the WIYN Tip-Tilt Module (WTTM)³, the 2.4m telescope at the MDM Observatory using the MDM Eight-K⁴, Echelle and RETROCAM⁵ (Morgan et al. 2005) imagers and the 6.5m Magellan Baade telescope using IMACS (Bigelow et al. 1999). A detailed discussion of our lensed quasar monitoring data reduction pipeline can be found in Kochanek et al. (2006), but we briefly summarize our technique here. We hold the lens astrometry fixed to the *HST H*-band measurements. We treat each quasar image as a point source and model the point-spread function with three nested, elliptical Gaussian profiles. We measure the flux of each image by comparison to the flux of 5 reference stars in the field. We assume that the lens galaxy flux remains constant and fix its value to the flux found by minimizing the residuals in a fit to the complete set of measurements from each instrument. We supplemented our optical lightcurves with *V*-band data published by Schechter et al. (1997). We applied magnitude offsets to the Schechter et al. (1997) data and data from the other observatories to match the *R*-band measurements from SMARTS. The wavelength differences between monitoring bands are small enough to have little effect on the

¹<http://cfa.harvard.edu/castles/>

²<http://www.astronomy.ohio-state.edu/ANDICAM/>

³http://www.wiyn.org/wttm/WTTM_manual.html

⁴<http://www.astro.columbia.edu/arlin/MDM8K/>

⁵<http://www.astronomy.ohio-state.edu/MDM/RETROCAM>

results given the expected $\lambda^{4/3}$ scaling of the optical accretion disk size (Shakura & Sunyaev 1973) and our measurement uncertainties.

PG 1115+080 is a particularly challenging system to monitor because the A1 and A2 images are separated by a mere $0''.48$. The seeing in our ground-based observations is rarely better than $1''.0$, so we were forced to sum the flux from A1 and A2 in most cases. We refer to this summed lightcurve as $A12 = A1 + A2$. On 22 nights (out of 123 total epochs) with exceptionally good seeing ($\lesssim 0''.7$) and dark skies, we were able to resolve the A1 and A2 images individually. The strongest effect of microlensing appears in the A1/A2 flux ratio, so the ability to resolve them, albeit sparsely, was important for breaking the degeneracies in the analysis. We present our optical monitoring data in Table 3.

We complement our optical lightcurves with X-ray fluxes from the two epochs of 0.5 – 8 keV *Chandra* imagery published by Pooley et al. (2006), although here we used the refined flux measurements presented in Pooley et al. (2007). The details of the X-ray data reduction and flux ratio calculations are found in those papers.

3. Microlensing Models

Microlensing statistics are strongly influenced by the presence of smoothly distributed dark matter (Schechter & Wambsganss 2002), typically parameterized as the ratio of the stellar surface density to the total surface density κ_*/κ . We considered a range of possible stellar mass fractions in our calculations. We used the *GRAVLENS* software package (Keeton 2001) to generate a series of ten models that match the *HST* astrometry and reproduce the mid-infrared ($11.7\mu\text{m}$) flux ratios from Chiba et al. (2005). Each model consists of concentric de Vaucouleurs and NFW (Navarro, Frenk & White 1996) profiles, and we vary the mass in the de Vaucouleurs component over the range $0.1 \leq f_{M/L} \leq 1.0$ in steps of $\Delta f_{M/L} = 0.1$, where $f_{M/L} = 1.0$ represents a constant mass-to-light ratio (de Vaucouleurs) model with no dark matter halo. Table 2 summarizes the microlensing parameters as a function of $f_{M/L}$. Treu & Koopmans (2002) found that the best fit to the system’s large stellar velocity dispersion ($\sigma_* = 281 \pm 25 \text{ km s}^{-1}$, Tonry 1998) is provided by a steep mass profile $\rho \propto r^{-2.35}$, implying a large stellar mass component, and for $H_0 = 72 \text{ km s}^{-1} \text{ Mpc}^{-1}$, the best fit to the (Schechter et al. 1997) time delays is provided by the $f_{M/L} = 0.8$ model.

We generated a set of microlensing magnification patterns at each image location for each of the 10 macroscopic mass models using a variant of the ray-shooting method (Schneider et al. 1992, see Kochanek 2004 for the details of our technique). The patterns are 8192×8192 images of the source-plane projection of the magnification patterns from an ensemble of

typical lens galaxy stars at each image location. We approximated the Galactic stellar mass function of Gould (2000) as a power law, assuming $dN(M)/dM \propto M^{-1.3}$ with a dynamic range in mass of a factor of 50. The mean stellar mass in the lens galaxy $\langle M \rangle$ is initially unknown, so magnification patterns are produced in units of the Einstein radius with an outer scale of $20 R_E$. For PG 1115+080, the Einstein radius is $R_E = 6.6 \times 10^{16} \langle M/M_\odot \rangle^{1/2}$ cm. To convert to physical units, all results are eventually scaled by some factor of $\langle M/M_\odot \rangle$. Henceforth, quantities in Einstein units will be given the “hat” accent to distinguish them from quantities in physical units. So the physical source size r_s is related to the scaled source size \hat{r}_s by $r_s = \hat{r}_s \langle M/M_\odot \rangle^{1/2}$, and the physical effective velocity v_e is related to the scaled velocity \hat{v}_e by $v_e = \hat{v}_e \langle M/M_\odot \rangle^{1/2}$.

In order to eliminate the quasar’s intrinsic variability, we shifted the optical light curves by the measured time delays (Schechter et al. 1997), so that any remaining variability in the flux ratios must be attributed to microlensing. It is impossible to offset the sparse X-ray flux measurements by the time delays, so we assume that X-ray flux ratios can be treated as simultaneous in a statistical sense. As described in § 2, we were forced to sum the flux from images A1 and A2 on all but 22 of the 123 total optical monitoring epochs.

As described in detail by Kochanek (2004) (see also Morgan et al. 2007; Poindexter, Morgan & Kochanek 2008), our Monte Carlo microlensing analysis searches for trajectories across the magnification pattern that fit the observed light curves. We used a thin accretion disk surface brightness profile for the source model (Shakura & Sunyaev 1973) with

$$I(R) \propto \left\{ \exp \left[(R/r_s)^{3/4} \right] - 1 \right\}^{-1}, \quad (1)$$

where the scale radius r_s is the radius at which the disk temperature matches the rest-frame wavelength of our monitoring band, $kT = hc(1 + z_s)/\lambda_{obs}$. We neglect the central hole in the emission profile, the effect of which is negligible at optical wavelengths. Microlensing primarily depends on the projected area of the source while the true scale lengths also depend on the shape of the source and its inclination. We will refer to a radius where we have ignored the shape and inclination of the source as an “effective” radius that defines a projected area πr_{eff}^2 . For a thin disk, the effective radius is related to the source scale length by $r_{eff}^2 = r_s^2 \cos i$ where i is the inclination angle. The X-ray emission presumably has a different emission profile and shape. Fortunately, Mortonson et al. (2005) demonstrated that the half-light radius measured with microlensing is essentially independent of the surface brightness profile, so we will characterize the X-ray emission by the effective half-light radius. For our thin disk model, the half-light radius is related to the disk scale length by $R_{1/2} = 2.44 r_s$. In summary, to compare the sizes of the optical and X-ray emitting regions we will use the ratio of the effective radii r_{opt}/r_X , to characterize the optical emission we will use the thin disk scale length $r_{s,opt}$ and an inclination angle $\cos i$, and for the X-ray emission we will use

the effective (i.e. no shape corrections) half-light radius $r_{1/2,X}$.

We generated 8 trial magnification patterns for each of the 10 macroscopic mass models. For each trial and model we produced 50,000 trial light curves for a 16×21 grid of X-ray and optical source sizes. These source sizes \hat{r}_s are scaled sizes that depend on the microlens mass $r_s = \hat{r}_s \langle M/M_\odot \rangle^{1/2}$. We used logarithmic grids spanning the region producing acceptable fits with a grid spacing of 0.2 dex. In total there were 4×10^6 trial light curves for each combination of X-ray and optical source sizes. When assessing the quality of our fits to the observed flux ratios, we allowed for only 0.1 mag of systematic uncertainty in the flux ratios of the macro models because the mid-IR flux ratios of Chiba et al. (2005) are a close approximation to the intrinsic flux ratios in this system. In selecting trial light curves we gave equal statistical weight to the optical data where A1 and A2 could not be separately measured, optical data where A1 and A2 could be separately measured, and the X-ray data so that we would isolate trials with reasonable fits to all three classes of data. The final goodness of fit was evaluated with a χ^2 fit to the light curves where all data have their true statistical weights and we discard all fits with $\chi^2/N_{dof} > 4.0$ as they make no significant contribution to the final Bayesian integrals (see Kochanek 2004). Figures 1 and 2 show two examples of good fits to the data. The stronger flux anomalies in the X-ray data force the X-ray source to be more compact than the optical, leading to the much larger variability predicted for the X-ray bands relative to the optical.

To convert the results to physical units, we must either assume a prior on the mean mass of the microlenses $\langle M \rangle$ or a probability distribution for the transverse velocity between source, lens and observer v_e since the scaled and actual velocities are related by $v_e = \hat{v}_e \langle M/M_\odot \rangle^{1/2}$. For a mean stellar mass prior, we assume $0.1 M_\odot \leq \langle M \rangle \leq 1.0 M_\odot$. We model the effective velocity of the system with three components. We set the velocity of the observer $v_o = 94 \text{ km s}^{-1}$ to be the projection of the CMB dipole velocity (Kogut et al. 1993) onto the lens plane. We calculate a one-dimensional stellar velocity dispersion in the lens galaxy of $\sigma_* = 220 \text{ km s}^{-1}$ based on the Einstein radius of its macroscopic mass model and we assume a lens galaxy peculiar velocity dispersion of $\sigma_p = 235/(1+z_l) \text{ km s}^{-1} = 179 \text{ km s}^{-1}$ (Kochanek 2004). In general these two methods give similar physical size estimates because the sizes depend only weakly on the mass scale $\langle M \rangle$. Microlensing depends only on the size and velocity of the source in Einstein units, $\hat{r}_s = r_s/\langle M/M_\odot \rangle^{1/2}$ and $\hat{v}_e = v_e/\langle M/M_\odot \rangle^{1/2}$. A given level of variability can be produced either by moving a small source slowly (both \hat{r}_s and \hat{v}_s small) or a large source rapidly (both \hat{r}_s and \hat{v}_s large) with (roughly) $\hat{r}_s \propto \hat{v}_e$. But the mass scale implied by a given Einstein velocity scales as $\langle M/M_\odot \rangle = (v_e/\hat{v}_e)^2$ so the dependence of the physical scale on the mass essentially cancels given some knowledge of the physical velocity v_e , with $r_s = \hat{r}_s \langle M/M_\odot \rangle^{1/2} \propto \langle M \rangle^0$ (see Kochanek 2004). The poor temporal overlap of the optical and X-ray light curves means that the differences between

the priors are larger than we have found for most other lenses (e.g. Morgan et al. 2007; Poindexter, Morgan & Kochanek 2008).

4. Results and Discussion

Figure 3 shows the ratio of the effective radii of the optical and X-ray sources where the effective radius should be viewed as the square root of the projected source area. The results depend little on whether we use the mass or the velocity prior, so we present quantitative results only for the mass prior. The advantage of the size ratio is that it has no direct dependence on the mass of the microlenses (in the sense that $\hat{r}_{opt}/\hat{r}_X = r_{opt}/r_X$). We find that $\log[r_{opt}/r_X] = 1.2_{-0.4}^{+0.7}$. Figure 4 shows the estimates for the physical sizes, where we show the inclination corrected disk scale length for the optical source and the effective half-light radius for the X-ray source. Recall from § 3 that the disk scale length is the point where the temperature equals the photon energy $kT = hc/\lambda_{rest}$ and that the effective half-light radius has no shape or inclination corrections. Thus, at $0.3\mu\text{m}$ or $T = 4.8 \times 10^4$ K, the disk scale length is $\log[(r_{s,opt}/\text{cm})\sqrt{\cos(i)/0.5}] = 16.2 \pm 0.3$, and in the (rest-frame) 1.4-21.8 keV band the effective X-ray half light radius is $\log(r_{1/2,X}/\text{cm}) = 15.3_{-0.6}^{+0.5}$. Without the mass prior there are occasional solutions with very high effective velocities and relatively large X-ray sources that produce the outlying, large source bump in Figure 4. A better-sampled X-ray light curve is needed to eliminate these solutions.

We can compare these size estimates to theoretical expectations given the estimated black hole mass of $1.23 \times 10^9 M_\odot$ from Peng et al. (2006) based on the quasar luminosity and the width of the Mg II ($\lambda 2798\text{\AA}$) emission line, where black hole mass estimates using this technique have a typical uncertainties of ~ 0.3 dex (see McLure & Jarvis 2002; Peng et al. 2006). Fig. 4 shows the gravitational radius $r_g = 1.9 \times 10^{14}$ cm for this mass, which is the innermost stable circular orbit for a maximally rotating Kerr black hole. For reference, we also plot the innermost stable circular orbit for a Schwarzschild black hole at $6r_g$. The optical emission comes from well outside the inner edge of the disk ($\sim 86r_g$), justifying our neglect of the inner edge of the disk in Eqn. 1. Thin disk theory (Shakura & Sunyaev 1973) predicts that the optical size for a face-on quasar radiating with 10% efficiency at the Eddington limit should be $\log[r_{s,opt}/\text{cm}] = 15.6$, and our black hole mass/accretion disk size scaling from Morgan et al. (2007) predicts a scale radius of $\log[(r_{s,opt}/\text{cm})\sqrt{\cos(i)/0.5}] = 15.8 \pm 0.3$. Thus, our current result is consistent with the Morgan et al. (2007) black hole mass/accretion disk size scaling and is slightly larger than the theoretical thin disk size (see Morgan et al. 2007, for a detailed comparison of microlensing disk size estimates in 11 systems). The far more compact X-ray emission comes from a region very close to the inner disk edge, with

a half-light radius of $\sim 10r_g$. This result seems to favor models with a smaller emission structure (e.g. Martocchia et al. 2002; Ghisellini et al. 2004; Hirose et al. 2004) and disfavor the standard disk-corona model (Haardt & Maraschi 1991; Merloni 2003) and others with an extended X-ray continuum emission region (e.g. Hawley & Balbus 2002).

We also obtain some information on the structure of the lens galaxy, as illustrated in Figure 5 where we show our estimates of the stellar fraction $f_{M/L}$. We do not find a strong peak in the $f_{M/L}$ distribution, but we do detect a weak trend favoring models with lower $f_{M/L}$ and a low stellar surface density (Fig. 5), as we would expect. Both the Schechter et al. (1997) time delays (see Kochanek 2002) and the Tonry (1998) velocity dispersion (see Treu & Koopmans 2002) require mass models with little dark matter near the radius of the lensed images (although see Romanowsky & Kochanek 1999 for examples of dynamical models consistent with both a significant dark matter halo and the high velocity dispersion). While Figure 5 is not conclusive, it is probable that with better X-ray light curves we will be able to measure $f_{M/L}$ and either confirm or reject the time delay and velocity dispersion measurements.

We are expanding our analyses to include all 10 lensed quasars with archival X-ray data (see Pooley et al. 2007) as well as three systems (HE 1104–1805, RX J1131–1231 and Q 2237+0305) where we have obtained X-ray light curves. For many of these systems (RX J1131–1231, Q 2237+0305, WFI J2033–4723, SDSS 0924+0219 and H 1413+117) we have optical light curves comparable to those used here (see Morgan et al. 2006; Dai et al. 2008), but for the remainder we will have to rely on sparse, archival optical data. The main challenge we face is that the computational intensity of modeling the two bands simultaneously is a significant bottleneck for completing the analyses. Nonetheless, we see no fundamental barriers to complementing our correlations between optical disk size and black hole mass (Morgan et al. 2007) with their X-ray equivalents. The pattern suggested by PG 1115+080 is that the X-ray continuum emission region tracks the inner edge of the accretion disk. We hope to determine if this model is universal.

CSK acknowledges support from NSF grant AST-0708082. This research made extensive use of a Beowulf computer cluster obtained through the Cluster Ohio program of the Ohio Supercomputer Center. Support for program HST-GO-9744 was provided by NASA through a grant from the Space Telescope Science Institute, which is operated by the Association of Universities for Research in Astronomy, Inc., under NASA contract NAS-5-26666.

Facilities: CTIO:2MASS (ANDICAM), Hiltner (RETROCAM), WIYN (WTTM), HST (NICMOS, ACS), CXO.

REFERENCES

- Ballantyne, D.R., Turner, N.J. & Young, A.J. 2005, *ApJ*, 619, 1028
- Bigelow, B.C., Dressler, A.M., Schechtman, S.A. & Epps, H.W. 1999, *Proc. SPIE*, 3355, 12
- Blackburne, J.A., Pooley, D. & Rappaport, S. 2006, *ApJ*, 640, 569
- Blaes, O. 2007, in *ASP Conf. Ser. 373, The Central Engine of Active Galactic Nuclei*, ed. L.C. Ho & J.-M. Wang (San Francisco: ASP), 75
- Chartas, G., Agol, E., Eracleous, M., Garmire, G., Bautz, M.W., & Morgan, N.D. 2002, *ApJ*, 568, 509
- Chartas, G., Eracleous, M., Dai, X., Agol, E., & Gallagher, S. 2007, *ApJ*, 661, 678
- Chiba, M., Minezaki, T., Kashikawa, N., Kataza, H. & Inoue, K.T. 2005, *ApJ*, 627, 53
- Dai, X., Chartas, G., Agol, E., Bautz, M.W., & Garmire, G.P. 2003, *ApJ*, 589, 100
- Dai, X. Kochanek, C.S., Chartas, G., Morgan, N.D. Morgan, C.W. & Garmire, G.P.. 2008, in preparation
- DePoy, D.L., Atwood, B., Belville, S.R., Brewer, D.F., Byard, P.L., Gould, A., Mason, J.A., O'Brien, T.P., Pappalardo, D.P., Pogge, R.W., Steinbrecher, D.P., & Tiega, E.J., 2003, *Proc. SPIE*, 4841, 827
- Fabian, A.C., Nandra, K., Reynolds, C.S., Brandt, W.N. Otani, C., Tanaka, K. Inoue, H. & Iwasawa, K. 1995, *MNRAS*, 277, L11
- Fabian, A.C. Vaughan, S., Nandra, K., Iwasawa, K., Ballantyne, D.R., Lee, J.C., De Rosa, A., Turner, A., Young, A.J. 2002, *MNRAS*, 335, L1
- Falco, E.E., et al. 2001, in *ASP Conf. Ser. 237, Gravitational Lensing: Recent Progress and Future Goals*, Ed. T.G. Brainerd & C.S. Kochanek (San Francisco: ASP), 25
- Ghisellini, G. Haardt, F. & Matt, G. 2004, *A&A*, 413, 535
- Gould, A. 2000, *ApJ*, 535, 928
- Haardt, F. & Maraschi, L. 1991, *ApJ*, 380, L51
- Haardt, F. & Maraschi, L. 1993, *ApJ*, 413, 507
- Hawley, J.F. & Balbus, S.A. 2002, *ApJ*, 573, 738

- Hirose, S., Krolik, J.H., De Villiers, J.-P. & Hawley, J.F. 2004, *ApJ*, 606, 1083
- Hirose, S., Krolik, J.H. & Stone, J.M. 2006, *ApJ*, 640, 901
- Hubeny, I., Agol, E., Blaes, O. & Krolik, J.H. 2000, *ApJ*, 533, 710
- Hubeny, I., Blaes, O., Krolik, J.H. & Agol, E. 2001, *ApJ*, 559, 680
- Impey, C.D., Falco, E.E., Kochanek, C.S., Lehár, J., McLeod, B.A., Rix, H.-W., Peng, C.Y. & Keeton, C.R. 1998, *ApJ*, 509, 551
- Iwasawa, K., Fabian, A.C., Young, A.J., Inoue, H. & Matsumoto, C. 1999, *MNRAS*, 306, L19
- Iwasawa, K., Lee, J.C., Young, A.J., Reynolds, C.S. & Fabian, A.C. 2004, *MNRAS*, 347, 411
- Jovanović, P., Zakharov, A.F., Popović, L.Č, Petrović, T. 2008, *MNRAS*, in press (astro-ph/08014473)
- Keeton, C.R. 2001, preprint, (astro-ph/0102340)
- Kochanek, C.S. 2002, *ApJ*, 578, 25
- Kochanek C. S. 2004, *ApJ*, 605, 58
- Kochanek, C.S. & Dalal, N. 2004, *ApJ*, 610, 69
- Kochanek, C.S., Morgan, N.D., Falco, E.E. McLeod, B.A., Winn, J. Dembicky, J. & Ketzeback, B. 2006, *ApJ*, 640, 47
- Kogut, A., et al. 1993, *ApJ*, 419, 1
- Lee, J.C., Iwasawa, K, Houck, J.C., Fabian, A.C., Marshall, H.L. & Canizares, C.R. 1999, *ApJ*, 570, L47
- Lehár, J., Falco, E.E, Kochanek, C.S., McLeod, B.A., Impey, C.D., Rix, H.-W., Keeton, C.R. & Peng, C.Y. 2000, *ApJ*, 536, 584
- Maraschi, L. & Tavecchio, F. 2003, *ApJ*, 593, 667
- Martocchia, A., Matt, G. & Karas, V. 2002, *A&A*, 383, L23
- McLure, R.J. & Jarvis, M.J. 2002, *MNRAS*, 337, 109
- Merloni, A. 2003, *MNRAS*, 341, 1051

- Morgan, N.D., Caldwell, J.A.R., Schechter, P.L., Dressler, A., Egami, E. & Rix, H.-W. 2004, *AJ*, 127, 2617
- Morgan, C.W., Byard, P.L., DePoy, D.L., Derwent, M., Kochanek, C.S., Marshall, J.L., O'Brien, T.P. & Pogge, R.P. 2005, *AJ*, 129, 2504
- Morgan, C.W., Kochanek, C.S. Morgan, N.D. & Falco, E.E. 2006, *ApJ*, 647, 874
- Morgan, C.W., Kochanek, C.S., Morgan, N.D. & Falco, E.E. 2007, *ApJ*, submitted, (astro-ph/07070305)
- Mortonson, M.J., Schechter, P.L. & Wambsganss, J. 2005, *ApJ*, 628, 594
- Navarro, J.F. Frenk, C.S. & White S.D.M. 1996, *ApJ*, 462, 563
- Nayakshin, S., Cuadra, J. & Springel, V. 2007, *MNRAS*, 379, 21
- Paraficz D., Hjorth J., Burud I., Jakobsson P., Elíasdóttir Á. 2006, *A&A*, 455, L1
- Peng, C.Y., Impey, C.D., Rix, H.-W., Kochanek, C.S., Keeton, C.S., Falco, E.E., Lehár, J. & McLeod, B.A. 2006, *ApJ*, 649, 616
- Poindexter, S. Morgan, N.D. & Kochanek, C.S. 2008, *ApJ*, 673, 34
- Pooley, D., Blackburne, Jeffrey, A., Rappaport, S., Schechter, P.L. & Fong, W.-F. 2006 *ApJ*, 648, 67
- Pooley, D., Blackburne, J. A., Rappaport, S. & Schechter, P.L. 2007 *ApJ*, 661, 19
- Romanowsky, A.J. & Kochanek, C.S. 1999, *ApJ*, 516, 86
- Schechter, P.L. et al. 1997, *ApJ*, 475, L85
- Schechter P. L., Wambsganss J. 2002, *ApJ*, 580, 685
- Schneider, P., Ehlers, J. & Falco, E.E. 1992, *Gravitational Lenses* (Berlin:Springer)
- Shakura, N.I. & Sunyaev, R.A. 1973, *A&A*, 24, 337
- Tonry, J.L. 1998, *AJ*, 115, 1
- Treu, T. & Koopmans, L.V.E. 2002, *MNRAS*, 337, L6
- Vaughan, S., Fabian, A.C., & Nandra, K. 2003, *MNRAS*, 339, 1237

Wambsganss, J. 2006, in Saas-Fee Advanced Course 33, Gravitational Lensing: Strong, Weak and Micro, ed. G. Meylan, P. Jetzer. & P. North, (Berlin:Springer), 453

Weymann, et al. 1980, Nature, 285, 641

Wyithe J. S. B., Turner E. L. 2001, MNRAS, 320, 21

Yoo, J., Kochanek, C.S., Falco, E.E. & McLeod, B.A. 2005, ApJ, 626, 51

Young, A. & Reynolds, C.S. 2000, ApJ, 529, 101

Table 1. HST Astrometry and Photometry of PG1115+080

Component	Astrometry		Photometry		
	ΔRA	ΔDec	H=F160W	I=F814W	V=F555W
A1	$1''.328 \pm 0''.003$	$-2''.034 \pm 0''.003$	15.71 ± 0.02	16.42 ± 0.02	16.90 ± 0.11
A2	$1''.477 \pm 0''.004$	$-1''.576 \pm 0''.003$	16.21 ± 0.02	16.85 ± 0.01	17.62 ± 0.09
B	$-0''.341 \pm 0''.003$	$-1''.961 \pm 0''.003$	17.70 ± 0.02	18.37 ± 0.01	18.95 ± 0.12
C	$\equiv 0$	$\equiv 0$	17.23 ± 0.03	17.91 ± 0.02	18.39 ± 0.06
G	$0''.381 \pm 0''.003$	$-1''.344 \pm 0''.003$	16.66 ± 0.04	18.92 ± 0.02	20.74 ± 0.03

Table 2. PG1115+080 Lens Galaxy Mass Models

$f_{M/L}$	Convergence κ				Shear γ				κ_*/κ			
	A1	A2	B	C	A1	A2	B	C	A1	A2	B	C
0.1	0.75	0.76	0.69	0.84	0.22	0.27	0.18	0.32	0.021	0.023	0.016	0.031
0.2	0.69	0.71	0.64	0.79	0.27	0.33	0.20	0.41	0.046	0.050	0.034	0.066
0.3	0.64	0.66	0.59	0.74	0.31	0.39	0.23	0.49	0.075	0.081	0.055	0.105
0.4	0.59	0.61	0.54	0.69	0.36	0.44	0.25	0.58	0.11	0.12	0.08	0.15
0.5	0.54	0.56	0.49	0.63	0.40	0.50	0.28	0.66	0.15	0.16	0.11	0.20
0.6	0.49	0.51	0.44	0.59	0.44	0.56	0.30	0.74	0.20	0.21	0.14	0.25
0.7	0.45	0.46	0.39	0.54	0.48	0.61	0.32	0.81	0.25	0.27	0.18	0.31
0.8	0.40	0.41	0.34	0.49	0.52	0.66	0.35	0.89	0.32	0.34	0.24	0.39
0.9	0.36	0.38	0.30	0.44	0.55	0.71	0.36	0.96	0.40	0.42	0.29	0.46
1.0	0.31	0.33	0.26	0.40	0.60	0.76	0.39	1.03	0.51	0.54	0.39	0.57

Note. — Convergence κ , shear γ and the fraction of the total surface density composed of stars κ_*/κ at each image location for the series of macroscopic mass models where $f_{M/L} = 1.0$ corresponds to a constant mass-to-light ratio model for the lens galaxy.

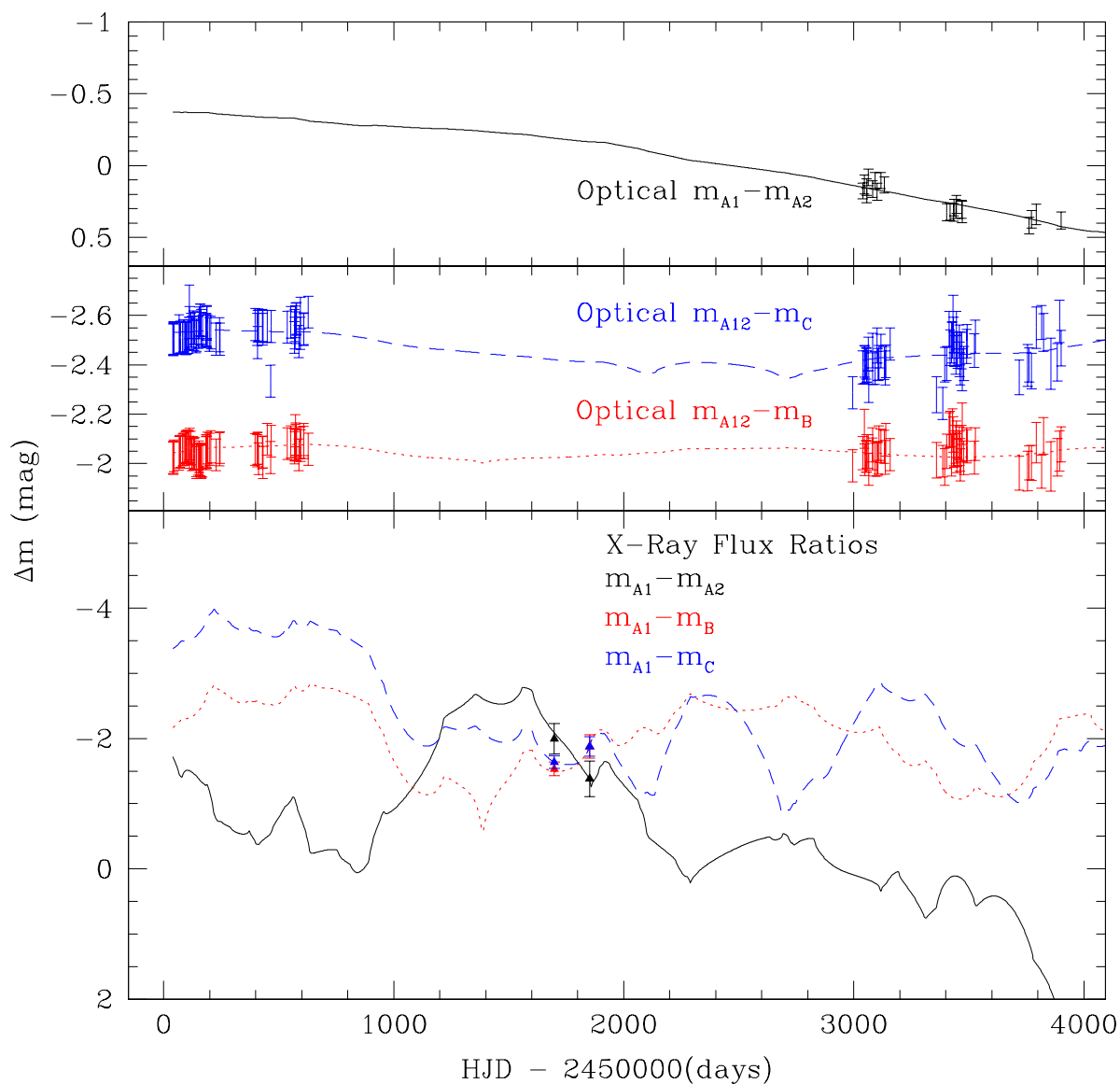


Fig. 1.— Examples of good fits to the observed flux ratios. Top panel: When resolvable, we fit the A1/A2 flux ratio individually. The error bars are the data, and the black curve is the fit. Middle panel: Dotted red and dashed blue curves are best fits to the A12/B and A12/C flux ratios, respectively. Data are plotted with error bars in the same color scheme. The A12/B and A12/C flux ratios varied little over the last decade. Bottom panel: The best fits to the observed A1/A2, A1/B, and A1/C X-ray flux ratios are plotted using solid black, dotted red and dashed blue curves, respectively. Data are plotted using triangular points in the same color scheme.

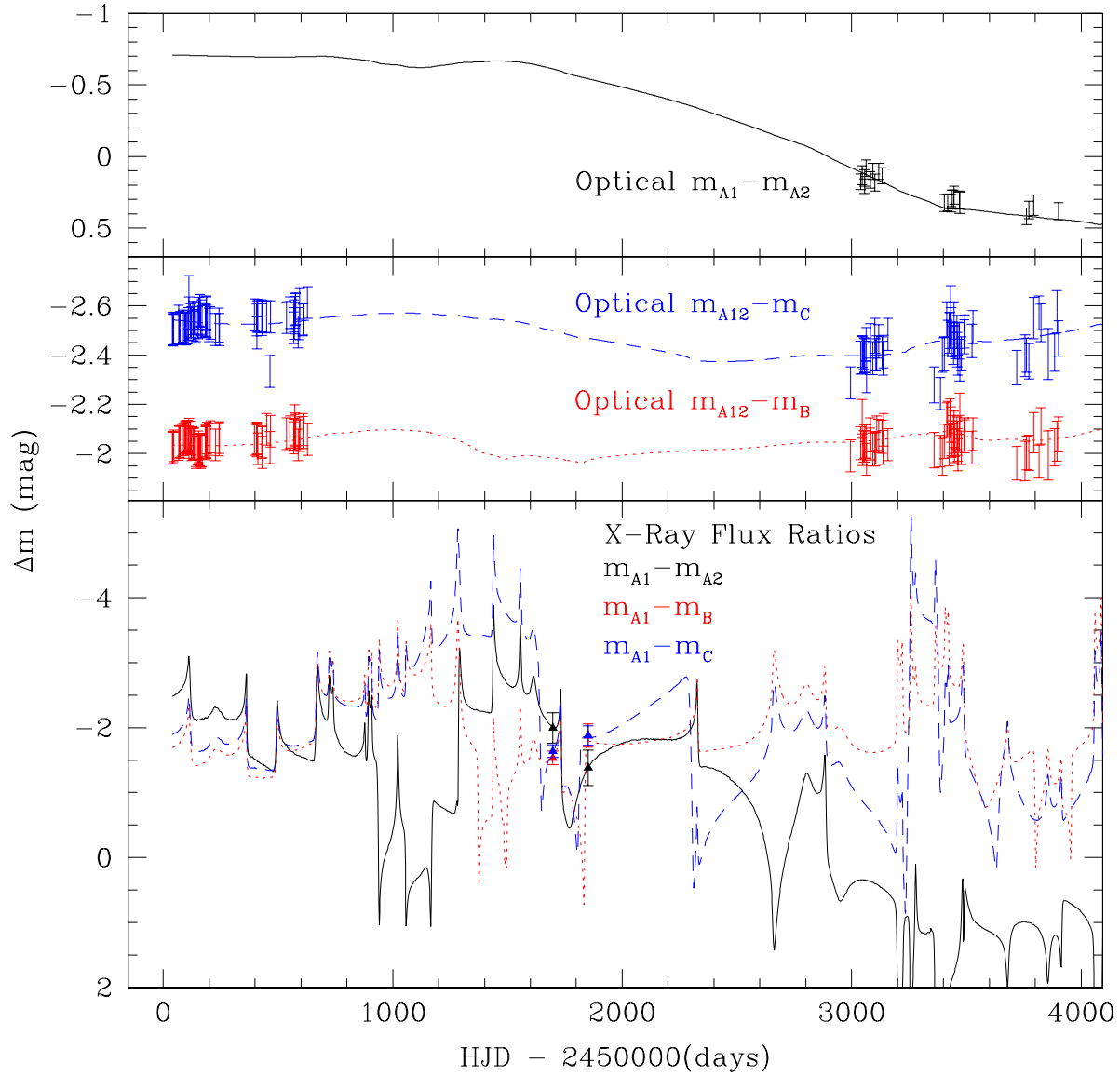


Fig. 2.— A second solution plotted as in Fig. 1. The very short timescale of the X-ray variability in this solution means that it has a higher effective velocity \hat{v}_e than the solution in Fig. 1.

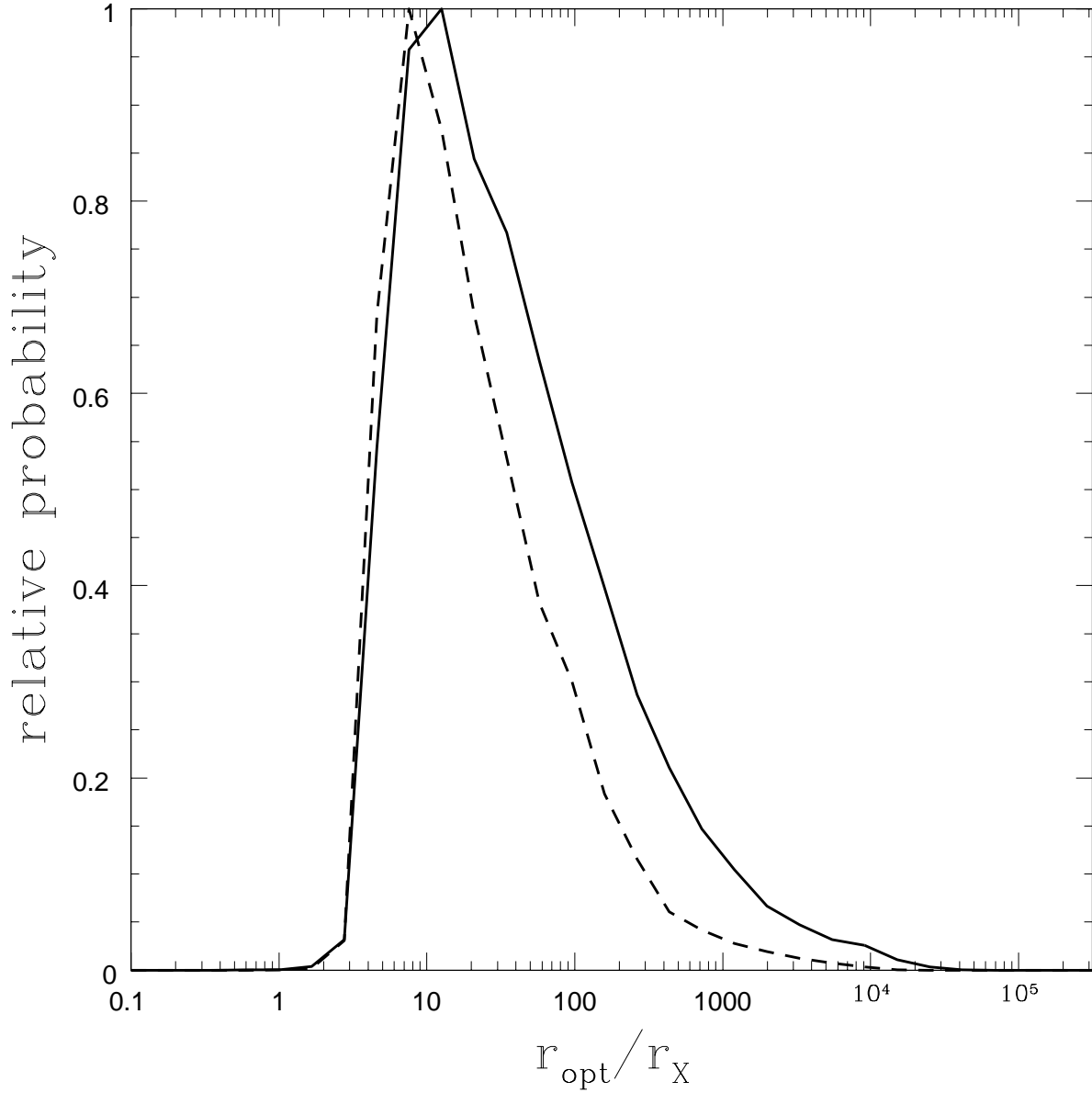


Fig. 3.— Probability distribution for the ratio of effective radii of the optical and X-ray sources. The solid curve uses the velocity prior. The dashed curve uses the prior on the microlens masses $0.1 M_{\odot} < \langle M \rangle < 1.0 M_{\odot}$.

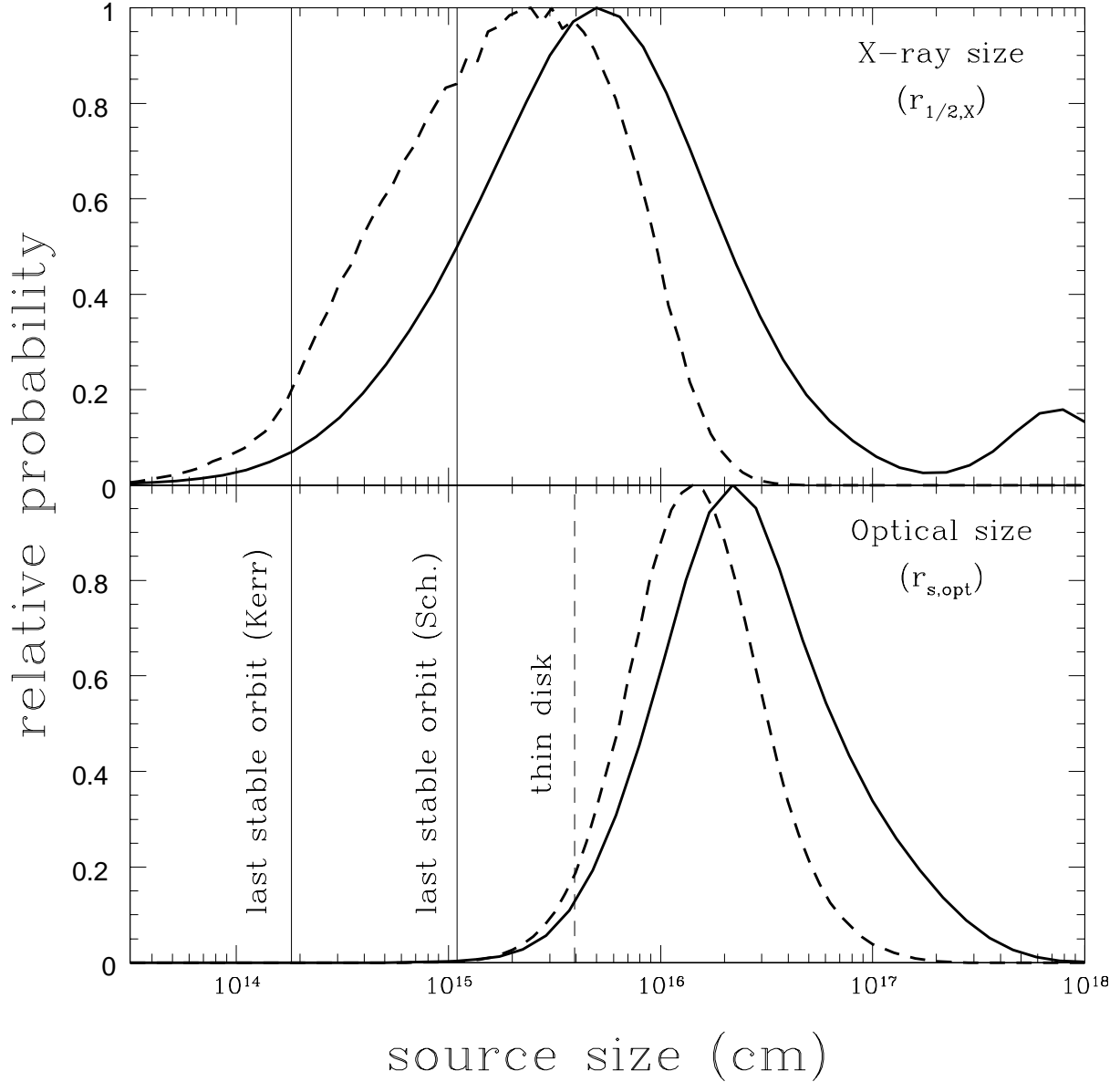


Fig. 4.— Probability distributions for the effective X-ray half light radius $r_{1/2,X}$ (top) and optical thin disk scale radius $r_{s,opt}$ (bottom). For the thin disk, we assumed an inclination of $\cos i = 1/2$. The solid curves use only the velocity prior while the dashed curves add the prior on the microlens masses of $0.1 M_{\odot} < \langle M \rangle < 1.0 M_{\odot}$. Given the black hole mass estimate of $1.23 \times 10^9 M_{\odot}$ for PG 1115+080 from Peng et al. (2006), the solid vertical lines indicate the innermost stable circular orbit $r_g = GM_{BH}/c^2$ for a maximally rotating Kerr black hole and the innermost stable circular orbit for a Schwarzschild black hole at $6r_g$. The dashed vertical line is the prediction of thin disk theory for the scale radius at $0.26 \mu\text{m}$ for an Eddington-limited accretion disk radiating at 10% efficiency.

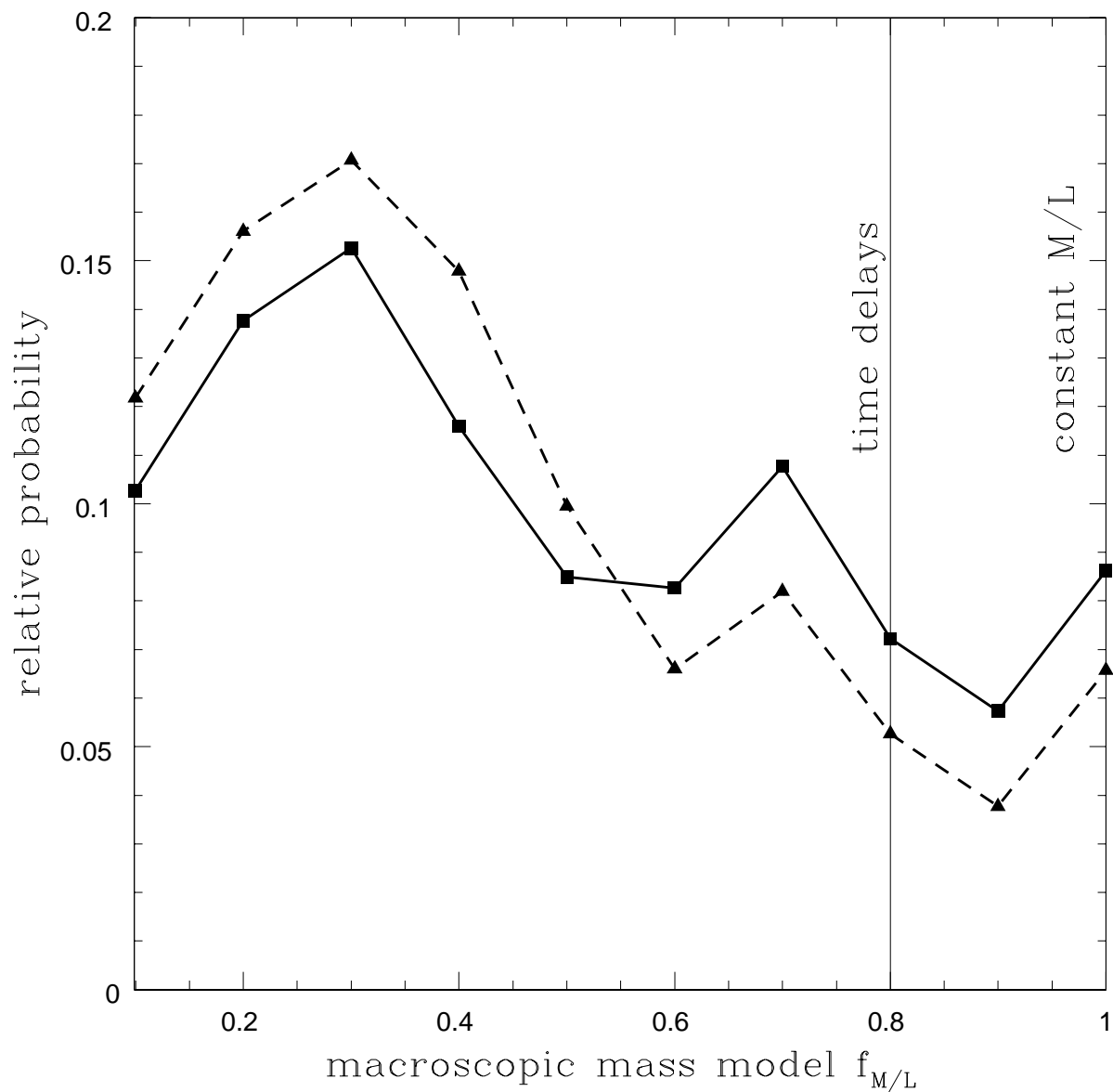


Fig. 5.— Probability distribution for $f_{M/L}$, the fraction of the lens galaxy mass in the constant M/L ratio (de Vaucouleurs) component. $f_{M/L}$ can be related to the stellar surface density fraction κ_*/κ at each image location using the data in Table 2. The $f_{M/L}$ value implied by the time delays is plotted with a solid vertical line.

Table 3. PG1115+080 Optical Light Curves

HJD	χ^2/N_{dof}	Image A1	Image A2	Image B	Image C	(Stars)	Source
2994.927	1.00	(-1.095 ± 0.006)	(-1.095 ± 0.006)	0.896 ± 0.008	1.192 ± 0.010	0.019 ± 0.004	MDM
3038.714	1.23	-0.227 ± 0.017	-0.403 ± 0.015	0.971 ± 0.010	1.319 ± 0.012	-0.014 ± 0.005	SMARTS
3045.790	1.18	-0.258 ± 0.029	-0.388 ± 0.026	1.064 ± 0.024	1.323 ± 0.018	-0.046 ± 0.005	SMARTS
3047.003	1.69	(-1.078 ± 0.004)	(-1.078 ± 0.004)	0.938 ± 0.007	1.336 ± 0.007	0.148 ± 0.004	WIYN
3055.690	1.46	-0.247 ± 0.018	-0.396 ± 0.016	0.973 ± 0.010	1.321 ± 0.012	-0.003 ± 0.004	SMARTS
3055.753	1.09	-0.219 ± 0.008	-0.425 ± 0.008	0.950 ± 0.007	1.314 ± 0.008	0.068 ± 0.004	MAGELLAN
3063.677	1.47	-0.288 ± 0.016	-0.369 ± 0.015	0.968 ± 0.009	1.362 ± 0.011	0.004 ± 0.004	SMARTS
3064.824	1.55	(-1.077 ± 0.005)	(-1.077 ± 0.005)	0.900 ± 0.007	1.235 ± 0.008	0.066 ± 0.004	MDM
3080.640	1.90	-0.246 ± 0.016	-0.409 ± 0.015	0.993 ± 0.009	1.374 ± 0.011	0.005 ± 0.004	SMARTS
3091.573	1.14	-0.273 ± 0.018	-0.376 ± 0.017	0.938 ± 0.010	1.309 ± 0.012	-0.006 ± 0.004	SMARTS
3101.647	1.11	-0.255 ± 0.023	-0.436 ± 0.020	0.918 ± 0.012	1.377 ± 0.017	-0.041 ± 0.005	SMARTS
3104.646	2.85	(-1.105 ± 0.004)	(-1.105 ± 0.004)	0.917 ± 0.007	1.297 ± 0.007	0.172 ± 0.004	WIYN
3108.540	3.46	(-1.119 ± 0.008)	(-1.119 ± 0.008)	0.964 ± 0.010	1.289 ± 0.012	0.000 ± 0.004	SMARTS
3116.582	1.02	-0.313 ± 0.019	-0.417 ± 0.018	0.953 ± 0.010	1.337 ± 0.013	-0.002 ± 0.004	SMARTS
3132.534	1.07	-0.286 ± 0.018	-0.419 ± 0.016	0.961 ± 0.010	1.300 ± 0.012	-0.021 ± 0.005	SMARTS
3136.717	5.84	(-1.132 ± 0.005)	(-1.132 ± 0.005)	0.893 ± 0.007	1.255 ± 0.008	0.062 ± 0.004	MDM
3138.476	1.34	(-1.093 ± 0.009)	(-1.093 ± 0.009)	1.004 ± 0.011	1.322 ± 0.013	-0.016 ± 0.005	SMARTS
3359.787	2.12	(-0.929 ± 0.011)	(-0.929 ± 0.011)	1.085 ± 0.011	1.350 ± 0.014	-0.006 ± 0.004	SMARTS
3368.759	0.66	-0.888 ± 0.023	-0.888 ± 0.023	1.251 ± 0.026	1.445 ± 0.034	-0.021 ± 0.005	SMARTS
3393.988	3.54	-0.163 ± 0.018	-0.064 ± 0.019	1.245 ± 0.009	1.690 ± 0.012	0.032 ± 0.004	retro0
3394.754	0.80	(-0.870 ± 0.015)	(-0.870 ± 0.015)	1.117 ± 0.031	1.531 ± 0.019	-0.040 ± 0.005	SMARTS
3403.785	1.00	0.076 ± 0.025	-0.248 ± 0.019	1.199 ± 0.011	1.555 ± 0.014	-0.011 ± 0.004	SMARTS
3413.792	2.84	(-0.850 ± 0.009)	(-0.850 ± 0.009)	1.286 ± 0.011	1.694 ± 0.014	0.001 ± 0.004	SMARTS
3417.760	1.55	0.092 ± 0.022	-0.228 ± 0.017	1.307 ± 0.015	1.637 ± 0.013	-0.019 ± 0.004	SMARTS
3424.727	0.60	(-0.818 ± 0.022)	(-0.818 ± 0.022)	1.216 ± 0.038	1.672 ± 0.035	-0.026 ± 0.005	SMARTS
3428.737	1.19	(-0.791 ± 0.014)	(-0.791 ± 0.014)	1.354 ± 0.031	1.709 ± 0.024	-0.042 ± 0.005	SMARTS
3431.786	1.51	(-0.836 ± 0.014)	(-0.836 ± 0.014)	1.282 ± 0.014	1.772 ± 0.020	-0.030 ± 0.005	SMARTS
3433.726	1.44	0.095 ± 0.022	-0.230 ± 0.017	1.230 ± 0.011	1.689 ± 0.015	-0.009 ± 0.004	SMARTS
3435.754	1.71	0.078 ± 0.019	-0.213 ± 0.015	1.224 ± 0.010	1.634 ± 0.013	0.006 ± 0.004	SMARTS
3442.691	2.05	0.079 ± 0.024	-0.220 ± 0.019	1.245 ± 0.011	1.607 ± 0.015	-0.010 ± 0.004	SMARTS
3445.734	2.31	0.051 ± 0.020	-0.219 ± 0.017	1.254 ± 0.011	1.696 ± 0.015	-0.005 ± 0.004	SMARTS
3447.633	0.82	(-0.833 ± 0.013)	(-0.833 ± 0.013)	1.199 ± 0.012	1.630 ± 0.017	-0.018 ± 0.005	SMARTS
3449.741	1.39	(-0.823 ± 0.010)	(-0.823 ± 0.010)	1.232 ± 0.011	1.630 ± 0.014	-0.013 ± 0.004	SMARTS
3458.682	0.96	(-0.819 ± 0.012)	(-0.819 ± 0.012)	1.264 ± 0.013	1.675 ± 0.017	-0.032 ± 0.005	SMARTS
3459.599	0.81	(-0.818 ± 0.015)	(-0.818 ± 0.015)	1.244 ± 0.014	1.604 ± 0.020	-0.030 ± 0.005	SMARTS
3461.676	0.86	(-0.825 ± 0.012)	(-0.825 ± 0.012)	1.211 ± 0.012	1.641 ± 0.016	-0.010 ± 0.005	SMARTS
3468.600	2.00	0.087 ± 0.021	-0.217 ± 0.017	1.253 ± 0.011	1.630 ± 0.014	-0.001 ± 0.004	SMARTS
3470.608	2.68	0.088 ± 0.026	-0.234 ± 0.020	1.324 ± 0.012	1.543 ± 0.015	-0.006 ± 0.004	SMARTS
3478.556	0.83	(-0.810 ± 0.014)	(-0.810 ± 0.014)	1.214 ± 0.013	1.595 ± 0.018	-0.033 ± 0.005	SMARTS
3483.539	1.05	-0.793 ± 0.017	-0.793 ± 0.017	1.677 ± 0.030	1.603 ± 0.026	-0.037 ± 0.005	SMARTS
3490.600	1.49	(-0.822 ± 0.011)	(-0.822 ± 0.011)	1.256 ± 0.011	1.653 ± 0.015	-0.013 ± 0.004	SMARTS
3491.594	1.34	(-0.808 ± 0.011)	(-0.808 ± 0.011)	1.263 ± 0.011	1.688 ± 0.015	-0.011 ± 0.004	SMARTS
3523.497	0.97	(-0.754 ± 0.012)	(-0.754 ± 0.012)	1.270 ± 0.012	1.703 ± 0.017	-0.017 ± 0.005	SMARTS
3527.474	1.20	(-0.761 ± 0.011)	(-0.761 ± 0.011)	1.318 ± 0.012	1.753 ± 0.016	-0.014 ± 0.005	SMARTS
3718.838	0.92	(-0.787 ± 0.015)	(-0.787 ± 0.015)	1.174 ± 0.013	1.562 ± 0.018	-0.024 ± 0.005	SMARTS
3737.018	4.71	-0.296 ± 0.008	0.060 ± 0.009	1.127 ± 0.007	1.434 ± 0.007	0.099 ± 0.004	MDM

Table 3—Continued

HJD	χ^2/N_{dof}	Image A1	Image A2	Image B	Image C	$\langle \text{Stars} \rangle$	Source
3750.790	0.68	-0.795 ± 0.022	-0.795 ± 0.022	1.331 ± 0.026	1.663 ± 0.035	-0.030 ± 0.005	SMARTS
3755.748	0.63	(-0.784 ± 0.023)	(-0.784 ± 0.023)	1.186 ± 0.024	1.613 ± 0.037	-0.020 ± 0.005	SMARTS
3761.765	1.09	0.160 ± 0.024	-0.257 ± 0.017	1.183 ± 0.010	1.579 ± 0.013	0.005 ± 0.004	SMARTS
3772.763	1.71	0.128 ± 0.021	-0.246 ± 0.016	1.175 ± 0.010	1.547 ± 0.013	0.007 ± 0.004	SMARTS
3792.766	2.47	0.091 ± 0.026	-0.249 ± 0.020	1.240 ± 0.012	1.706 ± 0.017	-0.006 ± 0.004	SMARTS
3815.678	1.48	(-0.851 ± 0.010)	(-0.851 ± 0.010)	1.116 ± 0.012	1.721 ± 0.017	-0.012 ± 0.005	SMARTS
3823.631	2.25	(-0.885 ± 0.013)	(-0.885 ± 0.013)	1.228 ± 0.013	1.646 ± 0.018	-0.016 ± 0.005	SMARTS
3855.526	0.59	(-0.883 ± 0.030)	(-0.883 ± 0.030)	0.996 ± 0.051	1.522 ± 0.058	0.023 ± 0.006	SMARTS
3884.450	1.00	(-0.908 ± 0.019)	(-0.908 ± 0.019)	1.118 ± 0.024	1.502 ± 0.024	-0.033 ± 0.005	SMARTS
3893.475	0.64	(-0.921 ± 0.025)	(-0.921 ± 0.025)	1.130 ± 0.022	1.655 ± 0.035	-0.032 ± 0.005	SMARTS
3900.490	0.94	0.041 ± 0.028	-0.341 ± 0.020	1.159 ± 0.012	1.548 ± 0.017	-0.023 ± 0.005	SMARTS

Note. — HJD is the Heliocentric Julian Day -2450000 days. The goodness of fit of the image, χ^2/N_{dof} , is used to rescale the formal uncertainties by a factor of $(\chi^2/N_{dof})^{1/2}$. The Image A1-C columns give the magnitudes of the quasar images relative to the comparison stars. The $\langle \text{Stars} \rangle$ column gives the mean magnitude of the standard stars for that epoch relative to their mean for all epochs. All A1 and A2 magnitudes in parentheses are the sum of the flux from both images. At these epochs the fluxes could not be measured individually.